Available online at www.sciencedirect.com
ScienceDirect
Magnetic Resonance Imaging 27 (2009) 834 – 844
MAGNETIC RESONANCE IMAGING

Remarks on *q*-space MR propagator in partially restricted, axially-symmetric, and isotropic environments

Evren Özarslan*, Cheng Guan Koay, Peter J. Basser

Section on Tissue Biophysics and Biomimetics, LIMB, NICHD, National Institutes of Health, Bethesda, MD 20892, USA

Received 3 September 2008; revised 29 November 2008; accepted 9 January 2009

Abstract

The problem of reconstruction of an apparent propagator from a series of diffusion-attenuated magnetic resonance (MR) signals is revisited. In nonimaging acquisitions, the inverse Fourier transform of the MR signal attenuation is consistent with the notion of an ensemble average propagator. However, in image acquisitions where one is interested in quantifying a displacement distribution in every voxel of the image, the propagator derived in the traditional way may lead to a counter-intuitive profile when it is nonsymmetric, which could be a problem in partially restricted environments. By exploiting the reciprocity of the diffusion propagator, an alternative is introduced, which implies a forward Fourier transform of the MR signal attenuations yielding a propagator reflected around the origin. Two simple problems were considered as examples. In the case of diffusion in the proximity of a restricting barrier, the reflected propagator yields a more meaningful result, whereas in the case of curving fibers, the original propagator is more intuitive. In the final section of the article, two more one-dimensional transformations are introduced, which enable the reconstruction of two- and three-dimensional propagators in, respectively, axially symmetric and isotropic environments — in both cases, from one-dimensional *q*-space MR data.
Published by Elsevier Inc.

Keywords: MR; MRI; Diffusion; PGSE; PFG; *q*-space; Propagator; Surface-normal; Curving fibers; Tractography; Axial symmetry; Isotropy; Restricted; Porous media

1. Introduction

Diffusion of molecules is an indirect yet powerful indicator of material and tissue microstructure. Pulsed-field-gradient (PFG) MR [1] is a convenient noninvasive method that can be used to observe diffusional motion of spin-bearing molecules such as endogenous water. The most commonly performed PFG-MR sequences involve the application of a pair of magnetic field gradient pulses around the 180° radiofrequency (RF) pulse in a spin-echo experiment. A spin that is moving between the application of these two pulses suffers a net phase shift. An ensemble of randomly moving molecules leads to an incoherent phase profile, which causes a decay in the acquired MR signal [2].

The attenuation of the MR signal can be changed by varying the experimental parameters, e.g., the magnitude and orientation of the diffusion gradients. This approach, sometimes referred to as *q*-space MR, enables the study of compartments whose dimensions are much smaller than the resolution achieved by MR imaging and microscopy. For example, the nonmonotonic dependence of the *q*-space signal on the wave number, *q*, [3,4] provides a direct means to determine microscopic compartment sizes.

To elucidate microstructural features of the specimen, one may fit physical models to the acquired *q*-space data. Alternatively, it was shown that the diffusion-attenuated MR signal profile can be transformed into a probability distribution function, hereafter referred to as the apparent propagator, quantifying the average probability for molecular displacements. The procedure for obtaining an apparent propagator from the MR signal was first proposed in Ref. [5]. The formalism was subsequently used to obtain symmetric apparent propagators in microporous zeolite crystallites [6]. It was shown that, in analogy with *k*-space MR imaging, the reconstructed propagator can be envisioned to be a "*q*-space image" of the displacements [7]. At around the same time,

* Corresponding author. Tel.: +1 301 435 1567; fax: +1 301 435 5035.
E-mail address: evren@helix.nih.gov (E. Özarslan).

0730-725X/$ – see front matter. Published by Elsevier Inc.
doi:10.1016/j.mri.2009.01.005

the PFG block was incorporated into nuclear magnetic resonance (NMR) microscopy sequences [8,9] that provided spatially localized displacement maps.

The q-space MR technique and the reconstructed apparent propagators have been used in a variety of contexts. For example, the reconstructed apparent propagator was shown to be a valuable marker of tissue microstructure [10]. In three-dimensional q-space acquisitions, the maxima of the orientation-dependent probabilities have been associated with the directions of white-matter fibers in the brain [11,12]. Descriptors of diffusion propagators, such as its moments and return-to-origin probability [13], are indicators of microstructure [14], which, in tissue, could be sensitive to changes due to aging, development and disease [15]. In disordered media, the q-space signal was used to estimate the propagator's scaling exponents that are related to the fractal dimension of the medium [16].

However, in this work, our focus is somewhat different from characterizing the microstructural features of porous media or tissue, although our findings may eventually be used in such studies. Instead, in more general terms, we discuss the propagators attainable from q-space MR and propose three new ways of obtaining propagators. After reviewing the notion of ensemble average propagators in the next section, we show that the meaning of the apparent propagator in MR imaging acquisitions is different from that in spectroscopic scans in the subsequent section. Consequently, a new notion of the apparent propagator for image acquisitions is introduced, which may be found useful in partially restricted environments. In a later part of the article, we consider one-dimensional q-space sampling performed on axially symmetric and isotropic environments and derive the corresponding transformations of the one-dimensional signals into two- and three-dimensional propagators, which are subsequently shown to be geometrically more meaningful than their one-dimensional counterparts.

2. Background

In a nonimaging PFG-MR signal acquisition, when the diffusion gradient pulses are infinitesimally short, the proton MR signal is given by [5]

$$S(\mathbf{q},\Delta)=\int_{\Re^3} d\mathbf{x}_0\,\rho(\mathbf{x}_0)\times\int_{\Re^3} d\mathbf{x}_1\,e^{-i2\pi\mathbf{q}\cdot(\mathbf{x}_1-\mathbf{x}_0)}K(\mathbf{x}_0;\mathbf{x}_1,\Delta), \tag{1}$$

where $\rho(\mathbf{x}_0)$ is the spin density at time t=0, which is typically equal to a constant over the entire region chemically connected to the region from which the signal is to be acquired, and is zero elsewhere. $K(\mathbf{x}_0;\ \mathbf{x}_1,\Delta)$ denotes the propagator indicating the probability that a spin initially situated at location $\mathbf{x}_0$ will have moved to location $\mathbf{x}_1$ after a time interval Δ. Finally, $\mathbf{q}=\gamma\delta\mathbf{G}/(2\pi)$ is an experimentally controlled vector, where γ is the gyromagnetic ratio, δ is the duration of the diffusion gradient pulses and $\mathbf{G}$ is the diffusion gradient vector. Note that $S(\mathbf{q},\Delta)$ is equal to unity at $\mathbf{q}=\mathbf{0}$ when the entire specimen is contained within the coil's sensitivity region. Therefore, we can refer to $S(\mathbf{q},\Delta)$ as signal attenuation and denote it by $E(\mathbf{q},\Delta)$.

If we introduce a net displacement vector, $\mathbf{u}=\mathbf{x}_1-\mathbf{x}_0$, the signal attenuation is given by

$$E(\mathbf{q},\Delta)=\int_{\Re^3} d\mathbf{u}\,e^{-i2\pi\mathbf{q}\cdot\mathbf{u}}P_{sp}(\mathbf{u},\Delta), \tag{2}$$

where

$$P_{\mathrm{sp}}(\mathbf{u},\Delta)=\int_{\Re^3} d\mathbf{x}_0\,\rho(\mathbf{x}_0)K(\mathbf{x}_0;\ \mathbf{x}_0+\mathbf{u},\ \Delta) \tag{3}$$

is the apparent propagator, where the subscript "sp" refers to spectroscopic (nonimaging) acquisitions. Note that the above definition is consistent with the notion of an ensemble average propagator as $P_{\mathrm{sp}}(\mathbf{u},\Delta)$ indicates the average probability that the spins within the ensemble will undergo a displacement $\mathbf{u}$. Eq. (2) suggests that the spectroscopic ensemble average propagator can be obtained from the MR signal attenuation via an inverse Fourier transform,

$$P_{\mathrm{sp}}(\mathbf{u},\Delta)=\int_{\Re^3} d\mathbf{u}\,e^{i2\pi\mathbf{q}\cdot\mathbf{u}}E(\mathbf{q},\ \Delta). \tag{4}$$

3. New notions of the apparent propagator

In this section, we shall consider the diffusion-weighted imaging pulse sequence illustrated in Fig. 1. Repeating this acquisition, with varying orientations of the imaging gradients $\pm\mathbf{g}$ (depicted by gray boxes), enables one to reconstruct three-dimensional images of the specimen being examined. Repeated acquisition of such three-dimensional images with different diffusion-weighting gradients $\mathbf{G}$ (depicted by blank boxes) yields a series of

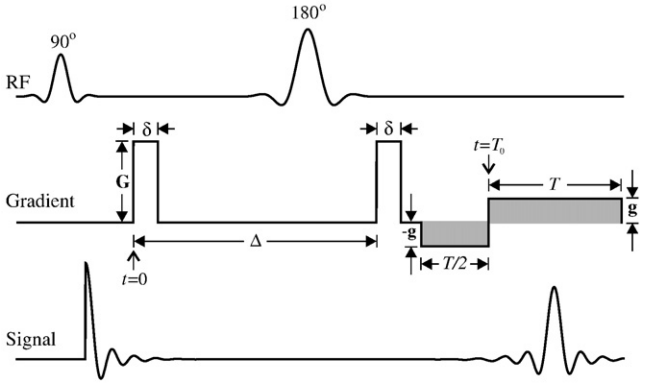

Fig. 1. A schematic of the diffusion-weighted pulsed field gradient spin echo imaging sequence. Repetition of the pulse sequence with varying $\mathbf{g}$ and $\mathbf{G}$ values; hence, sampling a six-dimensional space enables one to reconstruct three-dimensional displacement maps at each voxel of a three-dimensional image.

signals at each voxel location. The goal is to create a map of displacement distributions, each of which corresponds to a particular voxel [8,9]. Note that although simpler applications of diffusion-weighted acquisitions (without the application of ±**g** gradients) can be considered imaging [7] as well, for the purposes of this discussion, we don't refer to mapping displacements as imaging.

For the sake of simplicity, we shall assume that diffusion takes place only between the application of the two diffusion-sensitizing gradients, i.e., during the time interval Δ. Furthermore, we assume that the gradient pulses are infinitesimally narrow (δ→0) although the **q**-vector has finite magnitude.

The magnetization density immediately after the application of the second diffusion gradient is given by [17]

$$M(\mathbf{x}_1,\,\mathbf{q},\,\Delta)=\int_{\Re^3} d\mathbf{x}_0\;\rho(\mathbf{x}_0)e^{-i2\pi\mathbf{q}\cdot(\mathbf{x}_1-\mathbf{x}_0)}K(\mathbf{x}_0;\mathbf{x}_1,\Delta). \quad (5)$$

In our imaging experiment, this magnetization is subsequently encoded via the application of the frequency encoding gradients, ±**g**. If we define the quantity $\mathbf{k}(t)=(2\pi)^{-1}\gamma\mathbf{g}(t-T_0-T/2)$, where T is the duration of the acquisition, which starts at $t=T_0$, then the **k** — hence time — dependent signal from this pulse sequence is given by

$$\tilde{S}(\mathbf{k},\mathbf{q})=\int_{\Re^3} d\mathbf{x}_1 e^{-i2\pi\mathbf{k}\cdot\mathbf{x}_1}M(\mathbf{x}_1;\mathbf{q},\Delta), \quad (6)$$

where we do not explicitly write the Δ dependence of the signal for brevity. Note that this equation is different from the corresponding expressions in Refs. [8,9] in two respects. First, the Fourier kernels are the complex conjugate of those in these references, where the latter is consistent with a left handed coordinate system. Additionally, Refs. [8,9] seem to suggest that **k**-space encoding is performed on the spins at their initial ($t=0$) rather than final ($t=\Delta$, assuming no displacement after the application of the second diffusion gradient) positions.

When the inverse Fourier transform of both sides in Eq. (6) is taken via integrating over the variable **k**, the **q**-space signal at the voxel location **X** is given by

$$S(\mathbf{X},\mathbf{q})=\int_{\Re^3} d\mathbf{x}_0\;\rho(\mathbf{x}_0)e^{-i2\pi\mathbf{q}\cdot(\mathbf{X}-\mathbf{x}_0)}K(\mathbf{x}_0;\mathbf{X},\Delta). \quad (7)$$

An NMR signal attenuation can be defined by dividing the above expression by the signal $S(\mathbf{X},\mathbf{0})$, resulting in the expression

$$E(\mathbf{X},\mathbf{q})=\int_{\Re^3} d\mathbf{x}_0\;\rho_N(\mathbf{x}_0,\mathbf{X})e^{-i2\pi\mathbf{q}\cdot(\mathbf{X}-\mathbf{x}_0)}K(\mathbf{x}_0;\mathbf{X},\Delta), \quad (8)$$

where the normalized dimensionless spin density $\rho_N(\mathbf{x}_0,\mathbf{X})$ is defined through the relation

$$\rho_N(\mathbf{x}_0,\mathbf{X})=\frac{\rho(\mathbf{x}_0)}{\int_{\Re^3} d\mathbf{x}'\rho(\mathbf{x}')K(\mathbf{x}';\,\mathbf{X},\,\Delta)}. \quad (9)$$

Clearly, it is not possible to obtain the real propagator $K(\mathbf{x}_0;\,\mathbf{X},\,\Delta)$ from $S(\mathbf{X},\,\mathbf{q})$ data. However, an "effective" or "apparent" displacement probability distribution for each voxel can be defined by taking the Fourier transform of the $E(\mathbf{X},\,\mathbf{q})$ profile. As discussed in the Background section, the traditional way of obtaining such a distribution has involved the change of variables $\mathbf{u}=\mathbf{X}-\mathbf{x}_0$ and, subsequently, taking the inverse Fourier transform of the signal attenuations. We shall denote the resulting apparent propagator by $P_{\mathrm{im},1}(\mathbf{X},\,\mathbf{u})$, which is expected to represent the probability for spins within the voxel location **X** to undergo a displacement of **u** between the two diffusion gradients. The apparent propagator derived in the traditional way is then given by

$$\begin{aligned}P_{\mathrm{im},1}(\mathbf{X},\mathbf{u})&=\int_{\Re^3} d\mathbf{q}\;e^{i2\pi\mathbf{q}\cdot\mathbf{u}}E(\mathbf{X},\,\mathbf{q})\\&=\rho_N(\mathbf{X}-\mathbf{u},\,\mathbf{X})K(\mathbf{X}-\mathbf{u};\mathbf{X},\Delta).\end{aligned} \quad (10)$$

Note that, when we use the word "traditional," we do not refer to this particular form of the propagator. Rather, we refer to the method (the change of variables $\mathbf{u}=\mathbf{X}-\mathbf{x}_0$) that leads to this propagator.

Now, we shall do something different to Eq. (8). First, we restrict ourselves to diffusional motion only. In this case, the propagator, $K(\mathbf{x}_0;\,\mathbf{X},\,\Delta)$ is known to possess the reciprocity property [18], which ensures that

$$K(\mathbf{x}_0;\,\mathbf{X},\Delta)=K(\mathbf{X};\,\mathbf{x}_0,\Delta). \quad (11)$$

Plugging this expression into Eq. (8), and employing the change of variables $\mathbf{u}=\mathbf{x}_0-\mathbf{X}$, we obtain

$$E(\mathbf{X},\mathbf{q})=\int_{\Re^3} d\mathbf{u}\;\rho_N(\mathbf{X}+\mathbf{u},\,\mathbf{X})e^{i2\pi\mathbf{q}\cdot\mathbf{u}}K(\mathbf{X};\,\mathbf{X}+\,\mathbf{u},\,\Delta). \quad (12)$$

Consequently, another notion of apparent diffusional propagator is available through a forward Fourier transform of the $E(\mathbf{X},\,\mathbf{q})$ profile:

$$\begin{aligned}P_{\mathrm{im},2}(\mathbf{X},\mathbf{u})&=\int_{\Re^3} d\mathbf{q}\;e^{-i2\pi\mathbf{q}\cdot\mathbf{u}}E(\mathbf{X},\mathbf{q})\\&=\rho_N(\mathbf{X}+\mathbf{u},\mathbf{X})K(\mathbf{X};\mathbf{X}+\mathbf{u},\Delta).\end{aligned} \quad (13)$$

We will now examine Eqs. (10) and (13) and try to understand what the two definitions of the apparent propagators quantify. First, note that, in both cases, the apparent propagators are weighted by the normalized spin density

$$\rho_N(\mathbf{X}\pm\mathbf{u},\mathbf{X})=\frac{\rho(\mathbf{X}\pm\mathbf{u})}{\int_{\Re^3} d\mathbf{x}'\rho(\mathbf{x}')K(\mathbf{x}';\mathbf{X},\Delta)}, \quad (14)$$

where the + and − signs correspond to the apparent propagators derived in the new (by exploiting the reciprocity of the diffusion propagator) and traditional ways, respectively. The above expression suggests that instead of the initial spin density at the voxel location, the density at a distance ±**u** away from the voxel location is used, although its normalization is

performed by integrating the propagator at the actual voxel location (**X**).

Second, Eq. (10) suggests that the first notion of the apparent propagator is proportional to $K(\mathbf{X}-\mathbf{u}; \mathbf{X}, \Delta)$, which is the probability that a particle will undergo a displacement **u** before it arrives at the voxel location **X**. In contrast, the second notion of the propagator quantifies the probability that a particle situated at the voxel location will have moved a distance **u** away from the voxel location. Clearly, in most applications, the apparent propagator is expected to represent the likelihood for motion along different directions. When the motion along one direction is more likely than that along the opposite direction, e.g., due to a barrier on one side, we would like to assign larger probabilities to the direction of higher mobility. The first new notion of the apparent propagator quantifies the probabilities that results in the motion that brings the molecules to the voxel location. Therefore, if we visualize the propagator, for example, by vectors whose magnitude (length) represent the probability values, then the proper visualization of $P_{\mathrm{im},1}(\mathbf{X}, \mathbf{u})$ would involve "inward" vectors whose tips would be located at the voxel location and tails would be away from the center of the voxel. However, this is an unconventional representation. A more intuitive representation would employ "outward" vectors. This is implicitly assumed when white matter fiber orientations are depicted by orientation distribution functions. Therefore, we can expect the second new notion of the apparent propagator, $P_{\mathrm{im},2}(\mathbf{X}, \mathbf{u})$, to yield a more intuitive visualization of probabilities. By no means do we suggest that $P_{\mathrm{im},2}(\mathbf{X}, \mathbf{u})$ will always yield more meaningful results. For example, as detailed below, in the case of curving fibers, $P_{\mathrm{im},1}(\mathbf{X}, \mathbf{u})$ yields a more intuitive output. Moreover, as will be discussed in Discussion, $P_{\mathrm{im},2}(\mathbf{X}, \mathbf{u})$ is not defined for flow propagators, in which case the first new notion of the propagator yields correct and intuitive results.

Comparing the two new notions of the apparent propagator for imaging sequences, we note that the relation

$$P_{\mathrm{im},2}(\mathbf{X}, \mathbf{u}) = P_{\mathrm{im},1}(\mathbf{X}, -\mathbf{u}) \tag{15}$$

holds. This suggests that when diffusion is symmetric, the two results are identical. However, it is known that nonsymmetric diffusion propagators, i.e., complex-valued diffusion MR signals, are possible, e.g., when the spins are trapped within a Y-shaped object [19] and in partially restricted environments [20]. Some examples to other diffusion-related mechanisms that could lead to asymmetric propagators are treated next.

3.1. Diffusion in the proximity of a single infinite plate (1p)

As an example for a partially restricted environment, consider a very simple geometry where diffusion is impeded by an infinite impermeable plate located at X=0, which restricts the diffusing particles to the region X>0 as shown in Fig. 2A. For this geometry, the spin density is given by

$$\rho^{1\mathrm{p}}(X) = \rho\Theta(X), \tag{16}$$

where $\Theta(X)$ is the Heaviside theta function, which takes the value of 1 when its argument is greater than 0 and vanishes otherwise. This one-dimensional geometry was considered recently in Ref. [20], where, using the method of images, the propagator was shown to be given by

$$K^{1p}(x_0; X, \Delta) = \frac{1}{\sqrt{\pi}w}\left(e^{-(X-x_0)^2/w^2} + e^{-(X+x_0)^2/w^2}\right) \times \Theta(x_0)\Theta(X). \tag{17}$$

Here, w is a characteristic distance, defined by $w=(4D_0\Delta)^{1/2}$, where D_0 is the free space diffusion coefficient. Straightfor-

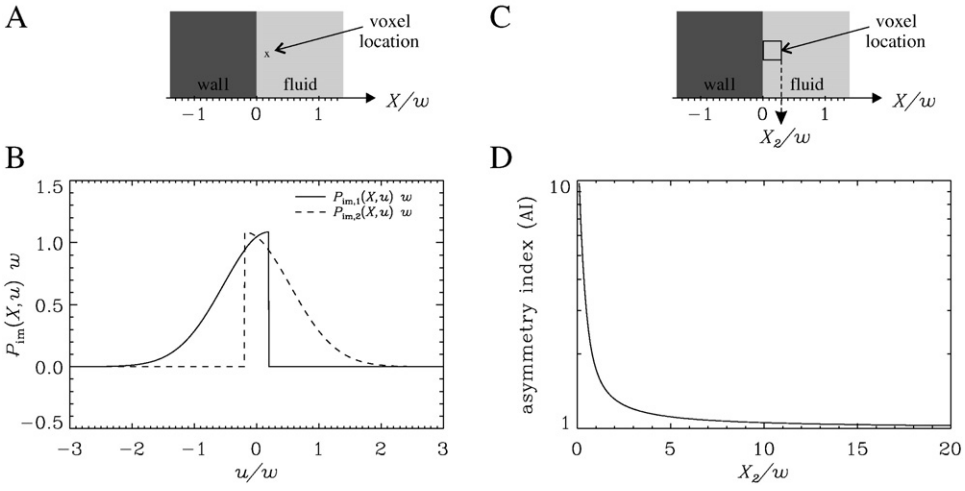

Fig. 2. (A) A sketch of the partially restricted geometry considered. The region X<0 is covered by a wall from which the spins that are diffusing in the region X>0 are reflected. The imaging voxel is situated at the location X=0.2w. (B) The apparent propagators reconstructed both in the traditional and new ways at the voxel location specified in Panel A. (C) The same geometry with a finite voxel size located adjacent to the wall extending to X_2. (D) The ratio of the integral of the propagator ($P_{\mathrm{im},2}$) over positive displacements to the integral over negative displacements from the voxel depicted in Panel C plotted as a function of the voxel size.

ward integration yields a simple expression for the normalized initial density, given by $\rho_N(x_0, X)=\Theta(x_0)$. Therefore, the two notions of apparent propagators are given by

$$\rho^{1p}_{\mathrm{im},1}(X,u)=\Theta(X-u)K^{1p}(X-u;X,\Delta), \tag{18}$$

and

$$\rho^{1p}_{\mathrm{im},2}(X,u)=\Theta(X+u)K^{1p}(X;X+u,\Delta), \tag{19}$$

respectively.

Fig. 2B illustrates these apparent propagators when the voxel is located very close to the wall at $X=0.2w$. It is clear that the propagator $P^{1p}_{\mathrm{im},1}(X, u)$ leads to a counter-intuitive picture in which displacements towards the wall appear to be finite, whereas displacements to the right are terminated although the wall is to the left of the voxel. The second notion of the propagator, however, has the more intuitive shape as the displacements through the wall are cut off.

Note that the treatment we have presented has not taken the finiteness of the voxel size into consideration so far. To account for imperfect resolution of the acquired images, we consider a voxel that starts at the wall–fluid interface and extends a distance X_2 into the fluid-filled region (see Fig. 2C). If we assume that all spins within the voxel contribute to the overall signal equally, we can simply integrate the expression for the magnetization density over the voxel. This procedure was performed in Ref. [20], and the relevant expressions will not be reproduced here. As discussed in Ref. [21], restrictions introduce diffusional anisotropy in the observed MR signal. Moreover, in Ref. [20], the anisotropy induced by the one-sided geometry treated here was considered and the effects of voxel size as well as the distance between the voxel and the wall was investigated. Since the same phenomenon is responsible for the asymmetry predicted here, we can expect to observe similar sensitivity of the asymmetry on the voxel size and location. However, the previous treatment considered only the magnitude of the signal, so the phase convention employed was arbitrary. Since using the correct phase convention is important for our application, we found it necessary to change the sign of the exponent in the Fourier kernel. Once the total signal profiles were computed up to voxels of size $X_2=20w$, we computed the Fourier transform of each of these profiles using the definition in Eq. (13). Next, an asymmetry index, defined by the expression

$$\mathrm{AI}([0,X_2])=\frac{\int_0^{\infty}P_{\mathrm{im},2}([0,X_2],u)du}{\int_{-\infty}^{0}P_{\mathrm{im},2}([0,X_2],u)du} \tag{20}$$

quantifying the level of asymmetry in the reconstructed apparent propagator, was evaluated. In the above expression $[0, X_2]$ denotes the voxel located between the points $X=0$ and $X=X_2$. In Fig. 2D, we plot this quantity against the voxel size. Although the asymmetry in the propagator quickly decays with increasing voxel size, there is some asymmetry even at the largest voxel size considered (AI≈1.03), which corresponds to 0.8 mm for $D_0=2\times10^{-3}$ mm^2/s and $\Delta=200$ ms. Note that as discussed in more detail in Ref. [20], the edge enhancement effect, manifested by a magnetization enhancement near the boundaries, helps the asymmetry prevail as the spins near the boundaries contribute more to the resulting signal.

These peculiar observations have quite significant implications when one deals with a diffusion-induced asymmetry in the propagator. For example, in fiber tractography, when branching fibers are encountered, the directions of the branches will be flipped when the first notion of the propagator is used, which can be appreciated by considering the meaning of $P_{\mathrm{im},1}(\mathbf{X}, \mathbf{u})$ as elucidated by Eq. (10). We note that although we discussed a semi-infinite space in this example, the findings of the above treatment will be valid when the spins are trapped within a confined domain and the voxel of interest is closer to one wall and sufficiently distant to others. Such a situation can be encountered in single cell microscopy [22] and in mapping the surface-normals of macroscopic interfaces [20].

3.2. Diffusion in curving fibers (cur)

Another interesting example that we consider is diffusion taking place inside curving fibers when the voxel contains a portion of the fiber. To simulate such a system, we take a circular loop whose thickness is assumed to be infinitesimal for simplicity. We shall suppose that our images are of dimension 2×2, where each pixel contains one of the quadrants of the loop yielding a fiber curving towards a different direction in each pixel. This geometry is illustrated in Fig. 3A.

The initial spin density for this geometry is given by

$$\rho^{\mathrm{cur}}(\mathbf{x}_0)=\frac{\delta(r_0-a)}{2\pi r_0}, \tag{21}$$

where r_0 and ϕ_0 denote the polar coordinates of $\mathbf{x}_0$, and the radius of the loop is denoted by a.

To find an expression for the propagator, we follow the procedure presented by Stephens [23], which yields

$$K^{\mathrm{cur}}(\mathbf{x}_0;\mathbf{x}_1,V)=\frac{\delta(r_1-r_0)}{\pi r_1}\times\left[\frac{1}{2}+\sum_{m=1}^{\infty}e^{-m^2V/2}\cos m(\phi_1-\phi_0)\right], \tag{22}$$

where r_1 and ϕ_1 denote the polar coordinates of $\mathbf{x}_1$ and V is a dimensionless variable quantifying the dispersion amount similar to the diffusion time; as $V\to0$, the propagator tends to a delta function, whereas as $V\to\infty$, it tends to a uniform distribution on the circle.

The magnetization density can be obtained by evaluating the integral in Eq. (5). The MR signal attenuation that originates from a pixel that contains the portion of the loop

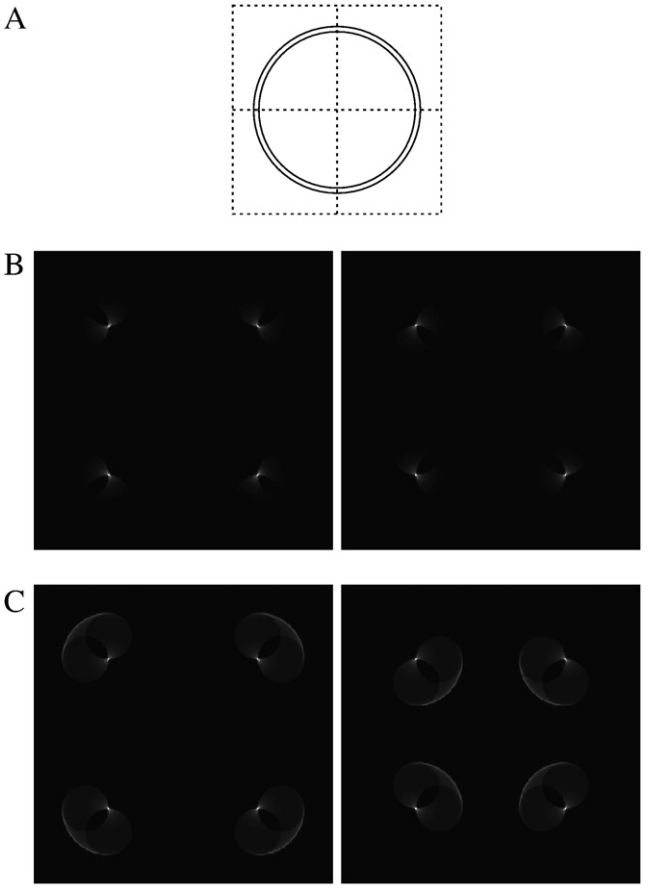

Fig. 3. (A) A sketch of the circular geometry considered. The dashed squares depict the four pixels of the image. Each quadrant of the circle lies within one of the pixels. (B) The reconstructed image of apparent propagators, $P_{\mathrm{im},1}$ (left) and $P_{\mathrm{im},2}$ (right), at relatively short diffusion times (V=0.5). (C) Same with panel b but with long diffusion times (V=5000).

between the angles θ_1 and θ_2 is obtained, after some algebra, to be

$$E^{\mathrm{cur}}([\theta_1,\theta_2],\mathbf{q}) = \frac{1}{2\pi}\int_{\theta_1-\phi_q}^{\theta_2-\phi_q} d\varphi e^{-i2\pi qa\cos\varphi}\left[J_0(2\pi qa) + 2\sum_{m=1}^{\infty} i^m e^{-m^2V/2}\cos(m\varphi)J_m(2\pi qa)\right], \quad (23)$$

where q and ϕ_q are the polar coordinates of $\mathbf{q}$, and J_m (.) is the m'th order Bessel function.

Evaluating this expression for a 129×129 matrix of q-space samples for each of the four pixels in our image, and subsequently taking the numerical Fourier transforms of the resulting two-dimensional q-space arrays, we obtain a 2×2 image of the apparent propagator that would result from curving fibers. Fig. 3B, C shows the apparent propagators, $P_{\mathrm{im},1}$ and $P_{\mathrm{im},2}$ obtained using Eqs. (10) and (13), depicted, respectively, on left and right columns. In this figure, Panel B was obtained by setting V=0.5 representing small diffusion time regime, whereas in Panel C, long diffusion time behavior, obtained by setting V=5000, is depicted.

Clearly in Panel B, high-intensity regions are restricted to the center of the displacement space. However, the long diffusion time regime shown in Panel C is more interesting where a distinct circular rim is observed in each pixel of the image. In the case of the first notion of the apparent propagator, this curve is almost identical to the portion of the loop that resides within the pixel. On the other hand, the second new notion of the apparent propagator results in rims that are located near the center of the entire image. Unlike in the problem of diffusion in the proximity of a single wall considered above, the first notion of the propagator yields a more intuitive output in the curving fiber geometry. Note that the images obtained are still consistent with the meanings attached to the two notions of the propagator by Eqs. (10) and (13), as discussed above.

4. The apparent propagator in axially-symmetric and isotropic environments

Frequently, the entire three-dimensional q-space is not sampled because of experimental limitations or because the desired characteristics of the specimen can be extracted from one-dimensional data, which can be obtained by applying diffusion gradients with increasing strength while keeping their direction fixed. The single infinite plate and curving fiber geometries treated above are examples to the class of problems in which the sampling of the three-dimensional q-space is not necessary. In this section however, we will tackle a different scenario in which the specimen exhibits certain levels of material symmetry such as full isotropy or axial symmetry.

Note that because of the symmetry in the considered problem, the reconstructed propagators are guaranteed to be symmetric. Consequently, the two notions of the apparent propagators discussed above are identical. Therefore, the subscripts of the apparent propagators will be replaced by those indicating the dimensionality of the space in which the propagator is reconstructed. Moreover, we consider a single voxel in the image or assume that the experiment is nonimaging; in either case, the geometry is assumed to be fully contained in the voxel or in the sensitivity region of the RF coil. Under these conditions, there is no need to include the voxel locations, and it is sufficient to write the displacement vector, which will hereafter be denoted by x, $\mathbf{r}$ and $\mathbf{R}$ in one, two and three dimensions, respectively.

When one-dimensional q-space data is available, the common approach to the reconstruction of an apparent propagator involves the evaluation of the expression

$$P_{1\mathrm{D}}(x) = \int dq\, e^{i2\pi qx}E(q), \quad (24)$$

where the x-axis is defined to be the direction of the diffusion gradients. For example, when the spins are trapped between two parallel infinite plates (pp), separated from each other by a distance L, with their normal vectors pointing along the x-axis, the expected signal intensity due to infinitesimally short

gradient pulses at long diffusion times ($D_0\,\Delta \gg L^2$) is given by [24]

$$E^{\mathrm{pp}}(q) = \frac{\sin^2(\pi q L)}{(\pi q L)^2}. \tag{25}$$

Here, the diffusion gradients are applied perpendicular to the infinite plates. The corresponding apparent propagator is

$$P_{1\mathrm{D}}^{\mathrm{pp}}(x) = \begin{cases} \dfrac{L-|x|}{L^2}, & |x| \le L \\ 0, & |x| > L \end{cases}. \tag{26}$$

As seen in Fig. 4A, this is just a triangular function.

However, when an axially symmetric or isotropic specimen is being evaluated, having one-dimensional $E(q)$ data is sufficient to reconstruct — perhaps more meaningful — two- and three-dimensional apparent propagators in cases of axial symmetry and isotropy, respectively. In this section, we derive the relevant transformations that relate the one-dimensional signal to higher-dimensional apparent propagators and compare these propagators to the one-dimensional propagator obtained via the inverse Fourier transform of Eq. (24).

4.1. Axially symmetric geometries

Many geometries of interest have an oblate or prolate structure, where the environment possesses a symmetry axis, which is the z-axis in our treatment. An example of such a diffusion process is Gaussian diffusion where two eigenvalues of the diffusion tensor are equal to each other. In such an axially symmetric (transversely isotropic) process, the $E(q)$ profile is the same when the diffusion gradient is applied in any direction (which defines the x-axis in our treatment) perpendicular to the symmetry axis. Therefore, a two-dimensional isotropic Fourier transform can be evaluated from one-dimensional q-space data. To this end, we shall start from the two-dimensional Fourier transform, given by

$$P_{2\mathrm{D}}(\mathbf{r}) = \int_{-\infty}^{\infty} dq_x \int_{-\infty}^{\infty} dq_y\, e^{i2\pi \mathbf{q}\cdot\mathbf{r}} E(q_x, q_y), \tag{27}$$

where the vectors $\mathbf{q}$ and $\mathbf{r}$ are two-dimensional and reside on the xy-plane; their radial and polar coordinates will be taken to be $(q,\ \theta_q)$ and $(r,\ \theta_r)$ respectively. By inserting the Rayleigh expansion for two-dimensional plane waves

$$e^{i2\pi \mathbf{q}\cdot\mathbf{r}} = \sum_{m=-\infty}^{\infty} i^m J_m(2\pi q r)\, e^{im(\theta_r - \theta_q)}, \tag{28}$$

into Eq. (27), it is straightforward to show that, in axially symmetric environments, the two-dimensional isotropic propagator is given by

$$P_{2\mathrm{D}}(r) = 2\pi \int_0^{\infty} dq\; q\; J_0(2\pi q r)\; E(q). \tag{29}$$

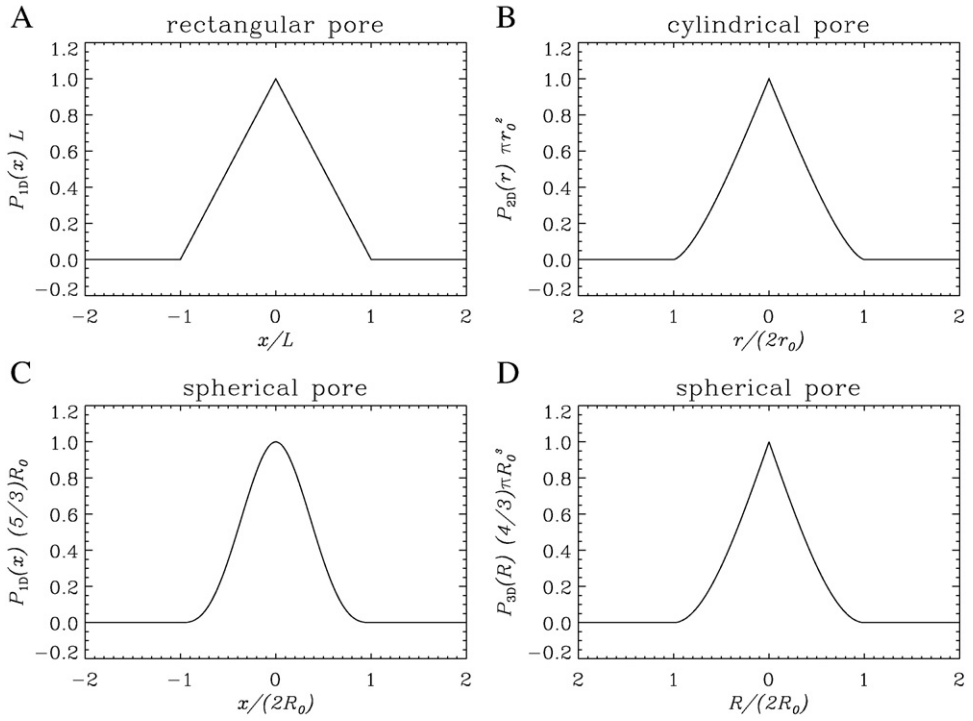

Fig. 4. The ensemble averaged propagators for the three closed geometries considered. (A) The propagator from parallel plate pores formed by two infinite parallel plates separated by a distance L. (B) The radial propagator of the cylindrical pore of radius r_0. (C) The one-dimensional propagator for the spherical pore of radius R_0. (D) The three-dimensional (radial) propagator of the spherical pore of radius R_0. In all cases, the diffusion time was taken to be very long ($D_0\,\Delta/L^2 \gg 1$, $D_0\,\Delta/r_0^2 \gg 1$, and $D_0\,\Delta/R_0^2 \gg 1$, where D_0 is the free space diffusion coefficient), and the duration of the diffusion pulses are assumed to be infinitesimally short. Note that the radial propagators in Panels (B) and (D) are not defined for negative radii. Therefore, to make comparisons with Panels (A) and (C) easier, the values to the left of the zero-displacement point are taken to be the replicates of those for positive radii.

The same analysis can be repeated for the forward Fourier transform, yielding essentially the same expression that transforms $P_{2D}(r)$ into $E(q)$. Clearly, the two-dimensional apparent propagator and the one-dimensional signal from axially symmetric regions are related to each other through the 0'th order Hankel transform.

The Fourier slice theorem implies that the one-dimensional average propagator, obtained from a one-dimensional Fourier transform, is related to the two-dimensional propagator via the relation

$$\begin{aligned} P_{1D}(x) &= \int_{-\infty}^{\infty} dy\, P_{2D}(x,y) \\ &= 2\int_{|x|}^{\infty} P_{2D}(r)\frac{r}{\sqrt{r^2-x^2}}dr, \end{aligned} \tag{30}$$

which is just the Abel transform [25] of $P_{2D}(r)$. Therefore, the two-dimensional axially symmetric propagator is given by the inverse Abel transform of the one-dimensional projection, i.e.,

$$P_{2D}(r) = -\frac{1}{\pi}\int_{r}^{\infty}\frac{P'(x)}{\sqrt{x^2-r^2}}dx. \tag{31}$$

4.1.1. The cylindrical pore at long diffusion times (cyl)

An example of a process with axial symmetry is restricted diffusion taking place inside a cylinder of radius r_0. The MR signal attenuation is given by [2]

$$E^{cyl}(q) = \left(\frac{J_1(2\pi q r_0)}{\pi q r_0}\right)^2. \tag{32}$$

The two-dimensional axially symmetric propagator can be evaluated by inserting Eqs. (32) into (29) and is given by

$$P_{2D}^{cyl}(r) = \begin{cases} \dfrac{4\cos^{-1}\left(\dfrac{r}{2r_0}\right) - \dfrac{r}{r_0}\sqrt{4-\left(\dfrac{r}{r_0}\right)^2}}{2\pi^2 r_0^2} & , r \le 2r_0 \\ 0 & , r > 2r_0 \end{cases}, \tag{33}$$

which is plotted in Fig. 4B.

4.2. Isotropic geometries

Porous materials that are the subjects of many MR-based studies are isotropic or lead to isotropic propagators due to the averaging process. In these environments, having the q-space data with diffusion gradients applied along any direction is sufficient to characterize the entire (three- dimensional) average propagator. The three-dimensional isotropic propagator can be reconstructed simply through the relationship

$$P_{3D}(R) = \frac{2}{R}\int_0^{\infty} dq\; q\; \sin(2\pi q R)\; E(q), \tag{34}$$

which is obtained by inserting the Rayleigh expansion of three-dimensional plane-waves [12] into the three-dimensional version of the Fourier transform relationship between E(**q**) and P(**R**) as in Eq. (4), where $q=|\mathbf{q}|$, $R=|\mathbf{R}|$ and **q** and **R** are three-dimensional vectors. Note that the relation between the three-dimensional isotropic propagator and one-dimensional propagator can be found by invoking the Fourier slice theorem,

$$\begin{aligned} P_{1D}(x) &= \int_{-\infty}^{\infty} dy \int_{-\infty}^{\infty} dz\; P_{3D}\left(\sqrt{x^2+y^2+z^2}\right) \\ &= 2\pi\int_0^{\infty} d\rho\; \rho\; P_{3D}\left(\sqrt{\rho^2+x^2}\right) \\ &= 2\pi\int_{|x|}^{\infty} dR\; R\; P_{3D}(R), \end{aligned} \tag{35}$$

where the changes of variables $\rho^2=y^2+z^2$ and $R^2=x^2+\rho^2$ were employed in the first and second steps, respectively. Differentiating both sides with respect to x and using the fundamental theorem of calculus, one gets

$$P_{3D}(R) = \left(-\frac{1}{2\pi x}\frac{dP_{1D}(x)}{dx}\right)\Bigg|_{x=R}. \tag{36}$$

4.2.1. The spherical pore at long diffusion times (sph)

When a PFG experiment is performed to observe diffusion inside a spherical pore of radius R_0, the MR signal attenuation, when the separation between the two diffusion sensitizing gradients is long, is given by [24]

$$E^{sph}(q) = \left[\frac{3}{(2\pi q R_0)^2}\left(\frac{\sin(2\pi q R_0)}{2\pi q R_0} - \cos(2\pi q R_0)\right)\right]^2. \tag{37}$$

The three-dimensional isotropic propagator can be evaluated by inserting Eq. (37) into (34) and is given by

$$P_{3D}^{sph}(R) = \begin{cases} \dfrac{3(2R_0-R)^2(4R_0+R)}{64\pi R_0^6} & , R \le 2R_0 \\ 0 & , R > 2R_0 \end{cases}. \tag{38}$$

The one-dimensional propagator can also be evaluated using a one-dimensional Fourier transform of E^{sph} (q) or by inserting Eq. (38) into Eq. (35), and is given by

$$P_{1D}^{sph}(x) = \begin{cases} \dfrac{3(2R_0-|x|)^3(4R_0^2+6R_0|x|+x^2)}{160R_0^6} & , |x| \le 2R_0 \\ 0 & , |x| > 2R_0 \end{cases}, \tag{39}$$

The one- and three-dimensional propagators are illustrated in Fig. 4C and D, respectively.

5. Discussion

In the first part of this article,, we showed that the apparent propagator, given by a Fourier transform of the MR signal attenuation, is proportional to a shifted normalized initial spin density and the real diffusion propagator. Both of these functions were shown to have two different meanings when the forward and backward Fourier transforms are

employed. In most cases, when the diffusion propagator is symmetric, and the spin density does not vary sharply within the length scale of the displacements, the two notions of the apparent propagator are identical. However, when the diffusional propagator is nonsymmetric, the reconstructed average propagators have quite different meanings. We have shown that, in situations where nonsymmetric propagators are encountered, such as in a partially restricted space, the reconstruction of the diffusional propagator that exploits its reciprocity property may lead to a more intuitive outcome.

As mentioned previously, the idea of an apparent propagator dates back to the 1960s, when Stejskal discussed the possibility of obtaining such a distribution from NMR data [5]. The expression he proposed, which is reproduced in the Introduction, has the same form as that which led to $P_{\mathrm{im},1}(\mathbf{X},\mathbf{u})$ in our treatment. Some of the subsequent works either assumed symmetric propagators [6] or started the analyses by using a phase change in the opposite sense to what applies to protons [8,9]. In the former reference, the Fourier transform is reduced to a cosine transform, and there is no difference between the forward and backward directions of the transform. In the latter references, which introduced spatially localized displacement mapping, because the treatment relating the MR signal to the propagator started with a sign change in the acquired phase, the same analysis as in Stejskal's work [5] led to the same form as that for $P_{\mathrm{im},2}(\mathbf{X},\mathbf{u})$ in our formulation. However, because of the assumption that k-space encoding is performed on spins at their initial positions, the meaning attached to the quantified propagators is different in Refs. [8,9]. One of the goals of this work was to shed some light on the apparent inconsistency in the literature regarding the phase conventions used in the estimations of the propagators from the MR signal intensity.

It is worth reiterating that, in the discussion that led to $P_{\mathrm{im},2}(\mathbf{X},\mathbf{u})$, we employed the reciprocity property of the real propagator. This is a fundamental property for diffusion propagators [18]; however, it may not hold for other types of transport processes. Other mechanisms that could lead to nonsymmetric propagators are flow and other types of coherent movements such as bulk motion. However, in these cases, the reciprocity property typically does not hold, and the second notion of the propagator $P_{\mathrm{im},2}(\mathbf{X},\mathbf{u})$ is invalid. For example the simplest flow propagator is given in terms of a Dirac delta function by

$$K^{\mathrm{flow}}(\mathbf{x}_0;\mathbf{X},\Delta)=\delta(\mathbf{X}-\mathbf{x}_0-\mathbf{v}\Delta), \tag{40}$$

where $\mathbf{v}$ is the velocity of the flowing particles. Clearly, such a propagator does not obey the reciprocity principle in Eq. (11), and as such, using the propagator $P_{\mathrm{im},2}(\mathbf{X},\mathbf{u})$ will yield incorrect results as it would imply that the flow occurs in the $-\mathbf{v}$ direction.

We would like to stress the other assumptions we employed in the derivations we presented in the first part of the article. First, for pedagogical purposes, the imaging part of the pulse sequence we considered was taken to be a three-dimensional radial $\mathbf{k}$-space acquisition where both lobes of the imaging gradients were applied after the diffusion gradients. Although the essential features of our findings are expected to be valid in most other imaging sequences, even a minor modification such as moving the first imaging gradient lobe to the proximity of the first diffusion gradient will alter the formalism. We showed that moving from spectroscopy to imaging necessitated a different interpretation for the reconstructed propagator. In a similar way, changing the imaging pulse sequence will typically require a reconsideration of the problem. The formulations we have presented in this article may serve as a guide in this endeavor. In fact, the dependence of the meaning attached to the propagators on the pulse sequence may be one of the factors that should be taken into consideration when designing diffusion-weighted imaging protocols.

For different pulse sequences, or when one is interested in incorporating diffusion taking place during the application of the diffusion and imaging gradients, the application of the multiple propagator formalism [4,26] to the imaging sequences [27] can be employed. Similarly, throughout the text, we did not discuss the effects of digitizing the echo. Consequently, all of the Fourier transforms, except those in the examples, were handled in the continuous domain. The truncation and finite sampling of the echo in general leads to a point spread function, which will yield an averaging of the signal over a region surrounding the voxel location; however, this would not change the conclusions of the analysis as demonstrated in the one-sided plate and curving fiber examples. As demonstrated above, although intravoxel averaging led to a rapid decay in the predicted level for diffusion asymmetry in the one infinite plate geometry, there was some significant residual asymmetry even when the voxel size was large (0.8 mm). In the case of curving fibers, the voxel size was the primary cause of asymmetry in the diffusion propagator because it is necessary for the fibers to change their orientations considerably within the voxel for this effect to be observable.

In the second part of the article, we considered apparent propagators obtained through a one-dimensional Fourier transform when the specimen under examination possessed axial symmetry or isotropy. Based on the realization that one-dimensional q-space data is sufficient to characterize higher-dimensional propagators, a library of relationships was derived between the one- and higher-dimensional propagators.

Simple geometries, such as infinite parallel plates, cylindrical pores and spherical pores at long diffusion times were considered as examples. The reconstructed probabilities were illustrated in Fig. 4. Restricted diffusion in the parallel plate pore geometry is manifested by a piecewise linear apparent propagator, which is not smooth at the origin. Similarly, almost linear two- and three-dimensional propagators were obtained in the axially-symmetric and isotropic environments, respectively. However, when a one-dimensional Fourier transform is employed, the propagator took a bell-shaped appearance (see Fig. 4C). This is an example in which the one-dimensional propagator obscured

some of the interesting features of the geometry. Therefore, it may be beneficial to apply the one-dimensional transformations of Eqs. (29) and (34), in respective cases of axial symmetry and isotropy, instead of the one-dimensional Fourier transform of Eq. (24).

Note that the NMR signal can be seen as the characteristic function of a phase distribution, i.e.,

$$S = \langle e^{i\phi} \rangle = \int d\phi \; e^{i\phi} \; p(\phi). \tag{41}$$

As discussed earlier, the phase acquired by a proton in a PFG experiment is $\phi = -i2\pi\mathbf{q}\cdot(\mathbf{x}_1 - \mathbf{x}_0)$. In one-dimensional q-space sampling, where the orientation of the $\mathbf{q}$-vector is held fixed along the x-axis, the phase is $\phi(x_0, x_1) = -i2\pi q(x_1 - x_0)$, or simply, $\phi(x) = -i2\pi qx$, where $x = x_1 - x_0$. Inserting this expression into the above integral, it is clear that the phase distribution, $p(\phi(x))$, is just the one-dimensional apparent propagator. The fact that a smoothed version of the propagator is obtained when a one-dimensional Fourier transform is applied to the signal from spherical pores is an indication that the violation of the Gaussian phase approximation is expected to be more severe in one-dimensional geometries (such as the parallel plate geometry); the smoothing effect due to the projection of the sharper high-dimensional propagator onto the gradient axis leads to a Gaussian-like phase dispersion in higher-dimensional isotropic environments.

Finally, since the propagator is the autocorrelation function of the pore shape function at long diffusion times, in closed pores, the zero-displacement probability is just the reciprocal of the pore "volume." As can be seen in Fig. 4A, B, and D, this was exactly the case for the zero-displacement values of the one-, two- and three-dimensional propagators for parallel plate, cylindrical and spherical pores, respectively. The $x=0$ values of the one-dimensional propagators for cylindrical and spherical pores suggest that there may not be such a shape-independent relation between the $P_{1D}(0)$ value of a higher-dimensional geometry and the shape of the pore, exemplifying the utility of the higher-dimensional propagators.

6. Conclusion

In conclusion, revisiting the problem of reconstruction of an apparent propagator from a series of diffusion-attenuated MR signals led to a new understanding of the apparent propagators in image acquisitions. In such scans, the propagator derived in the traditional way may lead to a counter-intuitive profile when the apparent propagator is not symmetric. An alternative definition was introduced obtained by exploiting the reciprocity property of the diffusion propagator, which implied a Fourier transform in the opposite sense leading to a propagator reflected around the origin. This new form of the apparent propagator was shown to be more meaningful in the problem of diffusion in the proximity of a restricting wall. However, in the problem of curving fiber and for flow propagators, the apparent propagator obtained using the traditional approach lead to more intuitive results.

In axially-symmetric and isotropic environments, we showed how one-dimensional q-space data can be used to reconstruct two- and three-dimensional apparent propagators that may yield information that could be obscured by a one-dimensional propagator. Also derived is a library of previously undocumented relationships between the one- and higher-dimensional propagators.

Acknowledgments

We would like to thank Drs. Maher Moakher and Denis Grebenkov for helpful discussions and Liz Salak for editing the manuscript. This research was supported by the Intramural Research Program of Eunice Kennedy Shriver National Institute of Child Health and Human Development, National Institutes of Health (NIH).

References

[1] Stejskal EO, Tanner JE. Spin diffusion measurements: spin echoes in the presence of a time-dependent field gradient. J Chem Phys 1965;42 (1):288–92.
[2] McCall DW, Douglass DC, Anderson EW. Self-diffusion studies by means of nuclear magnetic resonance spin-echo techniques. Ber Bunsenges Phys Chem 1963;67:336–40.
[3] Callaghan PT, Coy A, MacGowan D, Packer KJ, Zelaya FO. Diffraction-like effects in NMR diffusion studies of fluids in porous solids. Nature 1991;351:467–9.
[4] Özarslan E, Basser PJ. MR diffusion — "diffraction" phenomenon in multi-pulse-field-gradient experiments. J Magn Reson 2007;188(2): 285–94. URL http://dx.doi.org/10.1016/j.jmr.2007.08.002.
[5] Stejskal EO. Use of spin echoes in a pulsed magnetic-field gradient to study anisotropic, restricted diffusion and flow. J Chem Phys 1965;43 (10):3597–603.
[6] Kärger J, Heink W. The propagator representation of molecular transport in microporous crystallites. J Magn Reson 1983;51(1):1–7.
[7] Callaghan PT, MacGowan D, Packer KJ, Zelaya FO. High-resolution q-space imaging in porous structures. J Magn Reson 1990;90:177–82.
[8] Callaghan PT, Eccles CD, Xia Y. NMR microscopy of dynamic displacements: k-space and q-space imaging. J Phys E 1988;21:820–2.
[9] Callaghan PT, Xia Y. Velocity and diffusion imaging in dynamic NMR microscopy. J Magn Reson 1991;91:326–52.
[10] Cohen Y, Assaf Y. High b-value q-space analyzed diffusion-weighted MRS and MRI in neuronal tissues — a technical review. NMR Biomed 2002;15:516–42.
[11] Wedeen VJ, Hagmann P, Tseng WYI, Reese TG, Weisskoff RM. Mapping complex tissue architecture with diffusion spectrum magnetic resonance imaging. Magn Reson Med 2005;54(6):1377–86. URL http://dx.doi.org/10.1002/mrm.20642.
[12] Özarslan E, Shepherd TM, Vemuri BC, Blackband SJ, Mareci TH. Resolution of complex tissue microarchitecture using the diffusion orientation transform (DOT). Neuroimage 2006;31(3):1086–103. URL http://dx.doi.org/10.1016/j.neuroimage.2006.01.024.
[13] Hürlimann MD, Schwartz LM, Sen PN. Probability of return to origin at short times: a probe of microstructure in porous media. Phys Rev B 1995;51(21):14936–40.
[14] Mitra PP, Latour LL, Kleinberg RL, Sotak CH. Pulsed-field-gradient NMR measurements of restricted diffusion and the return-to-the origin probability. J Magn Reson 1995;114:47–58.
[15] Helmer KG, Meiler MR, Sotak CH, Petruccelli JD. Comparison of the return-to-the-origin probability and the apparent diffusion coefficient

of water as indicators of necrosis in RIF-1 tumors. Magn Reson Med 2003;49(3):468–78. URL http://dx.doi.org/10.1002/mrm.10400.

[16] Özarslan E, Basser PJ, Shepherd TM, Thelwall PE, Vemuri BC, Blackband SJ. Observation of anomalous diffusion in excised tissue by characterizing the diffusion-time dependence of the MR signal. J Magn Reson 2006;183 (2):315–23. URL http://dx.doi.org/10.1016/j.jmr.2006.08.009.

[17] Sukstanskii AL, Yablonskiy DA, Ackerman JJH. Effects of permeable boundaries on the diffusion-attenuated MR signal: insights from a one-dimensional model. J Magn Reson 2004;170:56–66.

[18] Beck JV, Cole KD, Haji-Sheikh A, Litkouhi B. Heat Conduction Using Green's Functions. Washington, DC: Hemisphere Publishing Corporation; 1992.

[19] Liu CL, Bammer R, Moseley ME. Generalized diffusion tensor imaging (GDTI): a method for characterizing and imaging diffusion anisotropy caused by non-Gaussian diffusion. Isr J Chem 2003;43(1–2):145–54.

[20] Özarslan E, Nevo U, Basser PJ. Anisotropy induced by macroscopic boundaries: surface- normal mapping using diffusion-weighted imaging. Biophys J 2008;94(7):2809–18. URL http://dx.doi.org/10.1529/biophysj.107.124081.

[21] Özarslan E, Basser PJ. Microscopic anisotropy revealed by NMR double pulsed field gradient experiments with arbitrary timing parameters. J Chem Phys 2008;128(15):154511. URL http://dx.doi.org/10.1063/1.2905765.

[22] Grant SC, Buckley DL, Gibbs S, Webb AG, Blackband SJ. MR microscopy of multicomponent diffusion in single neurons. Magn Reson Med 2001;46(6):1107–12.

[23] Stephens MA. Random walk on a circle. Biometrika 1963;50:385–90.

[24] Tanner JE, Stejskal EO. Restricted self-diffusion of protons in colloidal systems by the pulsed-gradient, spin-echo method. J Chem Phys 1968; 49(4):1768–77.

[25] Bracewell RN. The Fourier Transform and its Applications. New York: McGraw-Hill; 1978.

[26] Callaghan PT. A simple matrix formalism for spin echo analysis of restricted diffusion under generalized gradient waveforms. J Magn Reson 1997;129:74–84.

[27] Callaghan PT, Codd SL. Generalised calculation of NMR imaging edge effects arising from restricted diffusion in porous media. Magn Reson Imaging 1998;16:471–8.